*Sound & Vibration* 2026, 60(2), 4198.
doi: https://doi.org/10.59400/sv4198

Article

# Coupling vibration analysis for aerial inspection robot landing on transmission line under wind disturbance

**Xiaodong Zhang[1,2], Haiming Shen[1,3,*], Ahmad Bala Alhassan[4], Haibo Xu[1,2]**

[1] School of Mechanical Engineering, Xi'an Jiaotong University, Xi'an 710049, China
[2] Shaanxi Key Laboratory of Intelligent Robot, Xi'an Jiaotong University, Xi'an 710049, China
[3] College of Mechanical and Electrical Engineering, Shihezi University, Shihezi 832003, China
[4] School of Mechanical Engineering, Chulalongkorn University, Bangkok 10330, Thailand
*** Corresponding author:** Haiming Shen, shenhaiming13@163.com

**CITATION**

Zhang X, Shen H, Alhassan AB, et al. Coupling vibration analysis for aerial inspection robot landing on transmission line under wind disturbance. Sound & Vibration. 2026; 60(2): 4198. https://doi.org/10.59400/sv4198

**ARTICLE INFO**

Received: 11 March 2026
Revised: 10 April 2026
Accepted: 13 April 2026
Available online: 15 April 2026



**Abstract:** When the high-voltage transmission line inspection robot (HVTIR) lands amid wind disturbances, line vibrations significantly affect system stability. Therefore, this paper proposes a contact-force control strategy for HVTIR landing based on varying wind speed conditions: a nonlinear contact-force model is preferred for vibration reduction under low wind speeds, while a linear contact-force model enhances stability under medium and high wind speeds. Using a composite wind field model, the vibration bending beam model of the transmission line and the mass-stiffness-damping coupling model of the robot under wind disturbance were developed. An experimental verification system was established using wireless acceleration sensors. Results showed that under a typical low wind speed of 2 m/s, the exponential nonlinear contact-force strategy controlled vibration at 0.64 m/s$^2$, which was 90.1% more effective than direct loading. At a typical medium-high wind speed of 6 m/s, the experimental peak value using the linear contact-force strategy was reduced by 5.7% compared to the ideal peak value; the experimental RMS was reduced by 0.36%, and the linear contact-force strategy significantly reduced coupling vibrations. These experimental results demonstrate the reliability and applicability of the proposed control strategy, providing theoretical and technical support for the stable and rapid landing of the inspection robot.

**Keywords:** landing gripper; wind disturbance model; HVTIR-line coupled vibrations; exponential nonlinear contact-force model; contact-force strategy

## 1. Introduction

With the rapid increase in power transmission demand, intelligent and efficient inspection of high-voltage transmission lines has become a critical focus for the power industry. Currently, high-voltage transmission inspections (HVTIR) fall into two main categories [1–4].

Aerial inspection using UAVs enables rapid assessments; however, precision is constrained by safety distance requirements.

Ground-based inspection using walking robots offers high precision for close-range assessments but faces significant challenges in mounting and dismounting power lines. Additionally, these robots have low efficiency when overcoming large obstacles, especially transmission towers.

To address these challenges, our team has developed an HVTIR featuring hybrid flying, crawling, and gliding capabilities. This design effectively overcomes issues

such as low precision in aerial inspections, difficulty in mounting lines, and inefficiency in negotiating obstacles [5,6].

High-voltage transmission lines are often installed in harsh, inaccessible environments where wind causes significant disturbances, leading to vibrations, oscillations, and galloping of the lines. When the HVTIR transitions from flight mode to online mode, the coupling effect during contact between the line and the robot significantly affects the stability of this mode switch. Therefore, investigating contact force strategies between the flying inspection robot and the transmission line under wind disturbances, as well as mitigating coupling vibrations, is of paramount importance.

Chermprayong et al. [7], Suarez et al. [8], and Paul et al. [9] studied the interaction forces between a flying robot's manipulator end-effector and a target but neglected component deformation, using transfer matrices for force/torque control. Similarly, Li et al. [10] and Zhang et al. [11] investigated target manipulation by flying robots but disregarded the coupling forces at the end-effector, instead relying on visual servoing to adjust relative positions. These approaches generally depend on distance or visual sensors and overlook the coupling characteristics of contact forces, resulting in limited control precision.

In Meng et al.'s study [12], the contact force was simplified to a single stiffness-damping model for a rigid target. Wang et al. [13] treated the connection as a flexible beam to study the effects of vibration on the robot's pose. Khanmirza et al. [14] modeled the coupling as a rigid interaction, solved using rotor coordinate transformation. These studies either overlook the coupling characteristics or treat them as rigid connections. There is a lack of detailed research on the variation of coupling forces when the target is flexible, particularly in specific contexts.

The operation of flying manipulators is highly susceptible to wind disturbances. Existing research includes:

In the studies by Orozco Soto and Lippiello [15] and Acosta et al. [16], wind power spectral density estimation was used as a normalized transfer function to generate a white noise signal for processing during flying robot control. Ikeda et al. [17] converted wind speed into forces acting on the robot and examined the impact of wind disturbances on the robot's trajectory. Lee et al. [18] analyzed the influence of wind on the flying robot arm from a geometric perspective, primarily relying on disturbance observers and the robot's own pose sensors for trajectory planning, without considering disturbances from the operating object. Nava et al. [19] modeled wind disturbances as forces acting on a plane, neglecting the interaction laws between the robot and the target. Fang and Mao [20] and Zhang et al. [21] employed acceleration feedback enhancement controllers to compensate for wind disturbances. Liu and Huang [22] directly assessed the state through a sliding mode observer and controlled the disturbance using a corresponding sliding mode controller. Jiao et al. [23] utilized a sliding mode observer to evaluate the state and employed a backstepping attitude controller to attenuate disturbance effects. Bodie et al. [24] and Malczyk et al. [25] compensated for the dynamic coupling between the manipulator and UAV through visual tracking to address external disturbances such as wind.

Currently, controlling a flying robot to reach a target under wind disturbance typically relies on the robot's position and attitude sensing systems to determine its location, employs observers to counteract wind effects, or simplifies the wind as an external force without considering the coupling forces between the robot and the target. These approaches overlook the coupling effects between the flying robot and the target under wind disturbance, which reduces control accuracy and efficiency. Building on existing research, this paper develops a coupling model of the robot and the transmission line under wind disturbance and investigates the interaction forces at the contact point between the robot and the transmission line to achieve a smooth landing.

The innovative aspect of this study lies in applying both linear and nonlinear contact-force models of HVTIR under varying wind speed conditions, utilizing the established coupling model of the HVTIR line. This approach provides theoretical support for the stable landing of the flight inspection robot.

This paper is organized as follows: Section 2 presents the methods, including the coupled vibration model of the HVTIR line under wind disturbance. Section 3 covers the analysis, focusing on the contact-force model for various wind speeds through simulations. Section 4 discusses the results, detailing the contact force strategy verified experimentally. Section 5 summarizes the findings, and Section 6 concludes the paper.

## 2. Models and methods

### 2.1. Wind model

#### 2.1.1. Composition of the wind model

The wind model can be decomposed into several core components—namely, mean wind, gusts, turbulent (or fluctuating) wind, and wind shear—to facilitate the analysis of its deterministic behavior and stochastic disturbances. The standard decomposition formula for the engineering wind model is presented in Equation (1) [26].

$$\overrightarrow{V}_{wind}(t, \overrightarrow{x}) = \overrightarrow{V}_{mean}(\overrightarrow{x}) + \overrightarrow{V}_{gust}(\overrightarrow{x}) + \overrightarrow{V}_{turb}(t, \overrightarrow{x}) + \overrightarrow{V}_{shear}(\overrightarrow{x}) \quad (1)$$

$\overrightarrow{V}_{mean}(\overrightarrow{x})$: (Mean Wind): Refers to the average wind speed over a specific time interval (e.g., 10 min). It serves as the basis for structural design and wind energy assessment.

$\overrightarrow{V}_{gust}(\overrightarrow{x})$: (Gust): A phenomenon in which wind speed suddenly increases over a short period, typically a few seconds, is commonly described by the gust factor, represents the ratio of the gust speed to the mean wind speed.

$\overrightarrow{V}_{turb}(t, \overrightarrow{x})$: (Turbulent Wind): A random fluctuating component superimposed on the mean wind, characterized by high frequency and short periods, is the primary cause of structural vibrations and UAV jitter.

$\overrightarrow{V}_{shear}(\overrightarrow{x})$: (Wind Shear): This refers to the sudden and significant changes in wind speed and direction over a very short distance. If the UAV fails to adjust promptly, it can easily lose control or experience severe turbulence.

In engineering applications—particularly in UAV flight, transmission tower design, and wind load analysis—the mean wind and turbulent wind are the primary

factors considered.

a) Mean wind profile model

The mean wind is typically modeled as a constant vector or as a vector that varies slowly over time. Wind speed generally increases with altitude. Two primary models describe this vertical wind profile: the Power Law (Exponential Model) and the Logarithmic Law.

Exponential model (power law): $V(z) = V_{ref}(\frac{z}{z_{ref}})^{\alpha}$, $V(z)$ is the mean wind speed at height $z$, $V_{ref}$ is the wind speed at the reference height (typically 10 m), and $\alpha$ is the ground roughness exponent (approximately 0.1 over open water and up to 0.4 in city centers). The rougher the terrain, the larger the value of $\alpha$, resulting in a faster increase in wind speed with height. This model is suitable for neutral atmospheric conditions and flat terrain.

Logarithmic model: $V(z) = \frac{u_*}{k} ln(\frac{z}{z_0})$, where $u_*$ is the friction velocity, $k$ is the von Kármán constant ($\approx 0.4$), and $z_0$ is the surface roughness length. This model is particularly suitable for describing near-surface wind fields below 100 m.

b) Turbulent wind model

This model describes the law of energy distribution of turbulent wind as a function of frequency. It is used to simulate wind randomness and calculate structural dynamic responses. Common models include the Discrete Gust Model, the Dryden Model, and the Von Kármán Model (Spectral Models).

Discrete gust model: Used to simulate the most hazardous scenarios. A typical example is Equation (2):

$$V_{gust} = \frac{V_{max}}{2}(1 - cos\frac{\pi t}{T}) \tag{2}$$

This model simulates the complete impact process where wind speed rapidly rises from zero to a maximum value and then falls back. It is frequently employed for robustness testing of flight control systems.

Dryden/Von Kármán Models (Spectral Models): These describe wind energy distribution through Power Spectral Density (PSD) functions, representing the probability of gusts occurring at different frequencies.

Therefore, in this study, the wind force model is simplified as Equation (3):

$$\overrightarrow{V}_{wind}(t, \overrightarrow{x}) = \overrightarrow{V}_{mean}(\overrightarrow{x}) + \overrightarrow{V}_{turb}(t, \overrightarrow{x}) = V_{ref}(\frac{z}{z_{ref}})^{\alpha} + \frac{V_{max}}{2}(1 - cos\frac{\pi t}{T}) \tag{3}$$

### 2.1.2. Wind speed magnitude

When UAVs perform transmission line inspections, wind speeds exceeding 10 m/s significantly degrade their wind resistance capabilities and cause a sharp increase in battery consumption. Furthermore, maintaining image stability is becoming difficult. Therefore, to ensure both safety and inspection quality, the operating wind speed must be kept below 10 m/s; for mountainous terrain, this limit is stricter, typically below 7 m/s.

While 10 m/s is the safest limit for flight, operational standards are often more rigorous to meet the quality requirements of specific tasks.

Rapid inspection of corridor: This task primarily focuses on macro-level conditions within the line corridor, such as vegetation encroachment and external damage. Wind speeds up to 10 m/s are permissible for these operations.

Fine inspection (pin-level inspection) requires capturing clear images of micro-components such as insulators, fittings, and pins. High wind speeds induce high-frequency jitter in the fuselage, causing motion blur in long-focus lens imagery and preventing the identification of minute defects (such as missing split pins or cracks). Therefore, it is necessary to keep wind speeds under 8 m/s (or even lower, e.g., 6 m/s).

These constraints require that the wind speed range for the HVTIR in this study be between 0 and 6 m/s. Therefore, 2 m/s is selected as the typical low-speed wind speed in this research; 6 m/s is the typical medium-high wind speed.

## 2.2. Transmission line model

Since transmission lines and towers do not exist in isolation, this paper focuses specifically on the coupled vibration of the transmission line span between two towers to reduce the complexity of the study. High-voltage transmission lines can be arranged as single conductors, twin bundles, triple bundles, or quad bundles in power systems, and are often fitted with various hardware fittings. This study chooses a single conductor as the research object to simplify the model. The research's focus is on the coupled vibration of a single conductor between two Stockbridge dampers. **Figure 1** depicts the coordinate system for the coupled vibration system of the transmission line and the robot.

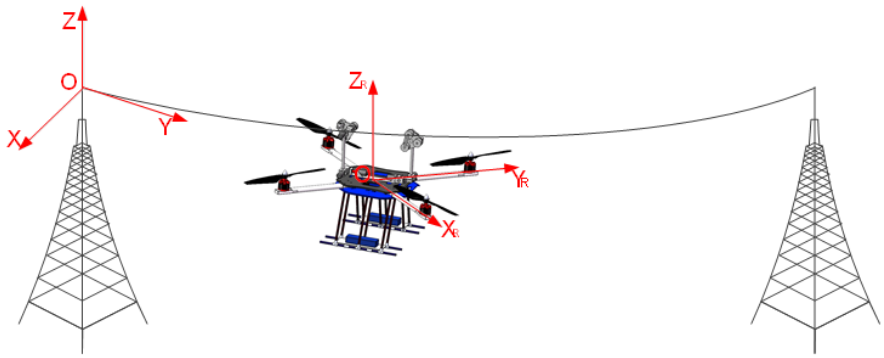


**Figure 1.** Coordinate system of the coupled transmission line-robot vibration system.

The wind speed range considered in this study is 0–6 m/s. For transmission lines, this corresponds to the regime of Aeolian vibration. This phenomenon involves the formation of alternating vortices shedding from the leeward side of the conductor, which generates periodic alternating lift forces. When the vortex shedding frequency approaches one of the natural frequencies of the conductor, resonance is triggered.

During Aeolian vibration, the transmission line acts as a flexible component characterized by low stiffness, long spans, large deflection, and high nonlinearity. Therefore, the transmission line can be idealized as a perfectly flexible structure that sustains tensile forces but resists neither compression nor bending moments. Its strain complies with Hooke's Law. Neglecting changes in the cross-sectional area, the

conductor can be modeled as a string or cable structure. However, when considering the bending stiffness of the transmission line, a tensioned curved beam model can be employed.

### 2.2.1. Transmission line string model

Catenary Curve Theory:

The transmission line is treated as a string fixed at both ends. Consider a differential segment $dx$ selected from the line. Assuming the linear density of the transmission line is $\rho(y)$, the mass of this segment is $\rho(y)dy$. Assuming the vertical displacement $z(y,t)$ is small, the partial differential equation for the vertical vibration of the transmission line is given as Equation (4) [27].

$$\rho(y)\frac{\partial^2 z(y,t)}{\partial t^2} - \frac{\partial}{\partial y}(T\frac{\partial z(y,t)}{\partial y}) = F(y,t)(0 < y < L) \tag{4}$$

Assuming the length of the transmission line is constant, the tension $T$ within the string is the mean tension, and the vertical displacement $z(y,t)$ is the variable, where $L$ is the length of the transmission line.

During Aeolian vibration, although the amplitude is small, the high-frequency vibration leads to variations in dynamic tension. Furthermore, the external load on the transmission line changes during the robot's landing process. Therefore, the dynamic tension under these conditions is expressed in Equation (5):

$$T = T_0 + \Delta T = T_0 + \frac{EA}{2L}\int_0^L (\frac{\partial z}{\partial y})^2 dy \tag{5}$$

Where: $T_0$ is the static tension of the transmission line. $\Delta T$ is the dynamic tension. $E$ is the elastic modulus of the conductor. $A$ is the cross-sectional area of the transmission line.

Defining the vibration boundary conditions at both ends of the transmission line as zero displacement, the vertical vibration model of the transmission line can be simplified to Equation (6):

$$\begin{cases} \rho(y)\frac{\partial^2 z(y,t)}{\partial t^2}dy - \frac{\partial}{\partial y}(T\frac{\partial z(y,t)}{\partial y})dy = F(y,t)dy(0 < y < L) \\ z(0,t) = z(L,t) = 0 \end{cases} \tag{6}$$

However, the string model cannot calculate curvature; consequently, it is unable to determine the bending stress at the conductor's clamps.

### 2.2.2. Ideal cable model

This model assumes that the conductor is perfectly flexible and possesses no bending stiffness, relying primarily on axial tension to provide the restoring force. The governing partial differential equation (PDE) is as Equation (7):

$$\begin{cases} \rho(y)\frac{\partial^2 z(y,t)}{\partial t^2} + c\frac{\partial z(y,t)}{\partial y} - \frac{\partial}{\partial y}(T\frac{\partial z(y,t)}{\partial y}) = F(y,t)(0 < y < L) \\ z(0,t) = z(L,t) = 0 \end{cases} \tag{7}$$

Where: $z(y,t)$ is the vertical vibration displacement of the conductor at position $y$ and time $t$; $\rho(y)$ is the linear density of the conductor; $c$ is the equivalent damping coefficient per unit length of the conductor (including structural damping and aerodynamic damping); $T$ is the mean axial operating tension of the conductor; $F(y,t)$ is the excitation force acting on the conductor per unit length (including wind force and the impact force from the robot landing); $x$ is the spatial coordinate along the span of the conductor; $t$ is time.

The ideal cable model does not account for bending stiffness; consequently, its accuracy decreases under the Aeolian vibration conditions of transmission lines.

#### 2.2.3. Bending beam model

Although the conductor behaves like a flexible cable in the mid-span, its bending stiffness has a significant impact on local stress and vibration modes at boundaries such as suspension clamps and Stockbridge damper installation points. Therefore, a more precise model introduces the bending stiffness term, forming the bending beam model.

The governing partial differential equation (PDE) for the bending beam model is as in Equation (8):

$$\begin{cases} \rho(y)\dfrac{\partial^2 z(y,t)}{\partial t^2} + c\dfrac{\partial z(y,t)}{\partial y} - \dfrac{\partial}{\partial y}(T\dfrac{\partial z(y,t)}{\partial y}) + EI\dfrac{\partial^4 z(y,t)}{\partial y^4} = F(y,t)(0<y<L) \\ z(0,t) = z(L,t) = 0 \end{cases} \tag{8}$$

Where: $E$ is the elastic modulus of the conductor; $I$ is the moment of inertia of the cross-section.

Consequently, this study adopts the bending beam model as the transmission line model.

### 2.3. Coupled vibration model during wind disturbance

#### 2.3.1. Transmission line model during wind disturbance

When the wind speed is within the range of 0.5–10 m/s, the conductor is subjected not only to aerodynamic drag on the windward side but also to the formation of a Kármán vortex street in the wake behind the conductor. This phenomenon induces periodic vibrations in the vertical plane. Although the amplitude of this vibration is relatively small (typically 1–3 times the conductor diameter), the frequency is high (3–150 Hz). Long-term exposure to such vibrations can lead to issues such as fatigue strand breakage, hardware fitting wear, and damper failure.

This study analyzes the wind forces acting on the transmission line under wind speeds of 0–6 m/s. The detailed analysis is illustrated in **Figure 2**.

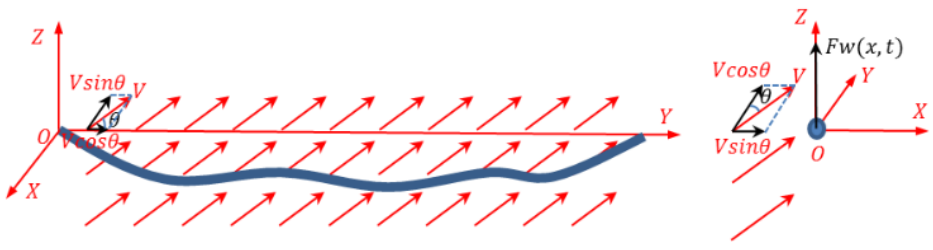


**Figure 2.** Analysis of wind forces acting on the transmission line.

The expression for the along-wind drag force is Equation (9).

$$F_{WD} = \frac{1}{2}\rho V^2 \mu_{SC} DBC_D \sin^2\theta \tag{9}$$

Where: $\rho$ is the air density, typically taken as 1.25 kg/m$^3$; $V$ is the wind speed; $\mu_{sc}$ is the shape coefficient of the transmission line. It should be taken as 1.2 when the conductor diameter is less than 17 mm or when icing occurs (regardless of diameter), and 1.1 when the diameter is greater than or equal to 17 mm; $D$ is the outer diameter of the transmission line; $B$ is the wind load amplification factor due to icing. It is taken as 1.1 for a 5 mm icing zone and 1.2 for a 10 mm icing zone; $C_D$ is the drag coefficient; $\theta$ is the angle between the wind direction and the transmission line.

The expression for the alternating lift force induced by wind is Equation (10).

$$F_W(y,t) = \frac{1}{2}\rho V^2 \mu_{SC} DBC_L \sin(\omega_s t + \Phi) sin^2\theta \tag{10}$$

The excitation frequency (i.e., the vortex shedding frequency) is determined by the Strouhal formula, which is Equation (11).

$$f_s = \frac{S * V}{D},\ \omega_s = 2\pi f_s \tag{11}$$

Where: $C_L$ is the dynamic lift coefficient; $f_s$ is the alternating vortex shedding frequency; $\omega_s$ is the angular frequency of alternating vortex shedding; $S$ is the Strouhal number, typically taken as 0.185–0.20 for cylinders; $\Phi$ is the initial phase angle.

Since the wind speed in this study is less than 8 m/s, which falls under the category of Aeolian vibration, the wind force model is simplified to account for the effects of mean wind and gusts on the transmission line. By substituting the formulas, the vibration model of the transmission line under wind force is obtained as Equation (12):

$$\begin{cases} \rho(y)\dfrac{\partial^2 z(y,t)}{\partial t^2} + c\dfrac{\partial z(y,t)}{\partial y} - \dfrac{\partial}{\partial y}\left(T\dfrac{\partial z(y,t)}{\partial y}\right) + EI\dfrac{\partial^4 z(y,t)}{\partial y^4} \\ = \dfrac{1}{2}\rho\left(V_{ref}\left(\dfrac{Z}{Z_{ref}}\right) + \dfrac{V_{\max}}{2}\left(1 - \cos\dfrac{\pi t}{T}\right)\right)^2 \sin^2\theta\, \mu_{SC} DB\left(C_D + C_L\sin(\omega_s t + \phi)\right) \quad (0 < y < L) \\ z(0,t) = z(L,t) = 0 \end{cases} \tag{12}$$

### 2.3.2. Analysis of HVTIR components during wind disturbance

The influence of wind on flying robots is a complex nonlinear aerodynamic problem. In a wind field, the total wind disturbance received by the flight inspection robot mainly consists of two parts: parasitic drag of the fuselage and rotor aerodynamic effects. The wind generates not only translational forces but also rolling moments [5, 28]. The schematic diagram of the coordinate system for the wind disturbance system acting on the robot is shown in **Figure 3**.

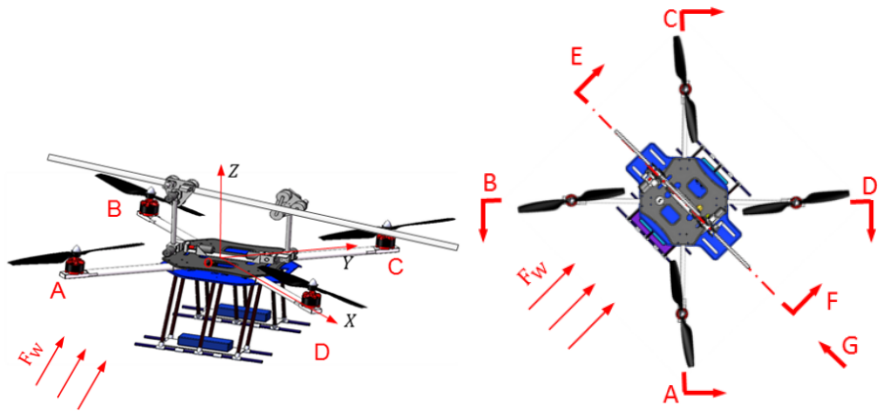


**(a)** Coordinate system of HVTIR and line coupling. **(b)** Schematic diagram of HVTIR section direction.

**Figure 3.** Coordinate system and sectional sketch of HVTIR landing flight under wind disturbance.

**a) Parasitic drag of the fuselage induced by wind**

The parasitic drag acting on the robot refers to the aerodynamic forces exerted on the robot's main body, rotor arms, grippers, gripper arms, and the plane formed by the rotating rotors.

Since the robot body and grippers are primarily subjected to planar forces, the calculation formula is as shown in Equation (13).

$$F_D = \frac{1}{2}\rho_A C_D S_{EQ} \left\| V_W - V_R \right\| (V_W - V_R) \tag{13}$$

Where: $F_D$ is the wind drag received by the planar components of the fuselage; its vector direction is consistent with the relative wind speed. $\rho$ is the air density, typically taken as 1.225 kg/m$^3$. $C_D$ is the drag coefficient of the various planar components of the fuselage. $S_{eq}$ is the equivalent windward projected area of the fuselage components. This represents the projected area of the components in the direction of the relative wind speed, which varies with the robot's tilt angle. $V_W$ is the absolute wind speed vector, representing the wind velocity in the world coordinate system. $V_R$ is the robot's moving speed vector. $V_{W\text{-}R}$ is the relative wind speed vector, which determines the actual wind speed and direction experienced by the robot during motion.

Since the rotor arms and gripper arms are primarily cylindrical, their calculation formulas refer to the wind disturbance formulas for transmission lines, as Equation (14):

$$F_{DR} = \frac{1}{2}\rho(V_{ref}(\frac{Z}{Z_{ref}}) + \frac{V_{\max}}{2}(1 - \cos\frac{\pi t}{T}))^2 \sin^2\theta_R D_R L_R (C_{DR} + C_{LR}\sin(\omega_{SR}t + \phi_R)) \tag{14}$$

Where: $\rho$ is the air density, typically taken as 1.25 kg/m$^3$. $\theta_R$ is the angle between the wind direction and the arm. $D_R$ is the outer diameter of the arm. $L_R$ is the length of the arm. $C_{DR}$ is the drag coefficient of the arm. $C_{LR}$ is the lift coefficient of the arm (typically $C_{LR}\approx C_{DR}$). $\omega_{SR}$ is the angular frequency of the alternating harmonic force caused by vortex shedding behind the arm. $\phi_R$ is the initial phase angle of the alternating harmonic force caused by vortex shedding on the arm.

**b) Aerodynamic effects of wind on HVTIR rotors**

When a crosswind blows across the high-speed rotating propellers of the robot, the resulting aerodynamic effects mainly include three types: the blade flapping effect, rotor-induced drag, and thrust variation.

In this study, the wind speed is low (0–6 m/s); therefore, the primary consideration is the thrust variation effect caused by the robot's inclination under crosswind conditions. Specifically, when there is a vector angle between the flight inspection robot and the wind force, the plane generated by the rotor's rotation will produce additional lift or drag under the influence of the wind. The calculation formula is as Equation (15):

$$F_{DR} = \frac{1}{2}\rho_A C_L S_{REQ} |V_W - V_R|^2 \tag{15}$$

Where: $C_L$ is the lift coefficient (typically $C_L \approx 0.5 C_D$); $S_{REQ}$ is the equivalent windward projected area of the propeller swept area.

### 2.3.3. Coupled model under wind disturbance

The analysis diagram of the Robot-Gripper-Line coupled model under wind disturbance in all directions is shown in **Figure 4**.

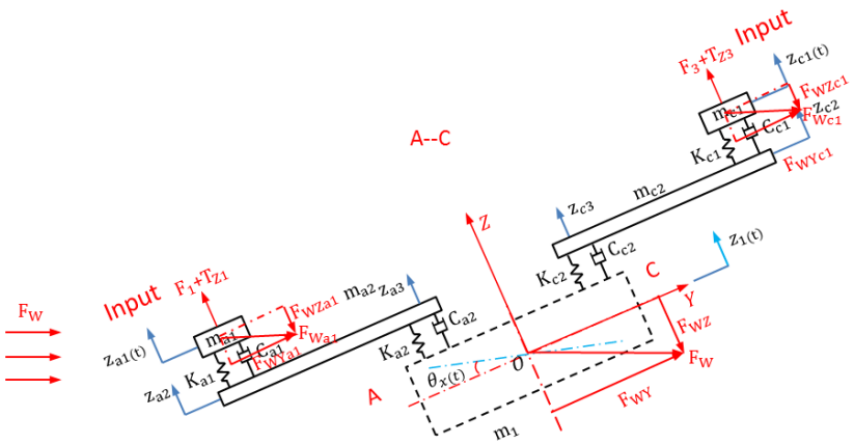


**(a)** Vibration model of HVTIR in the A-C section direction.

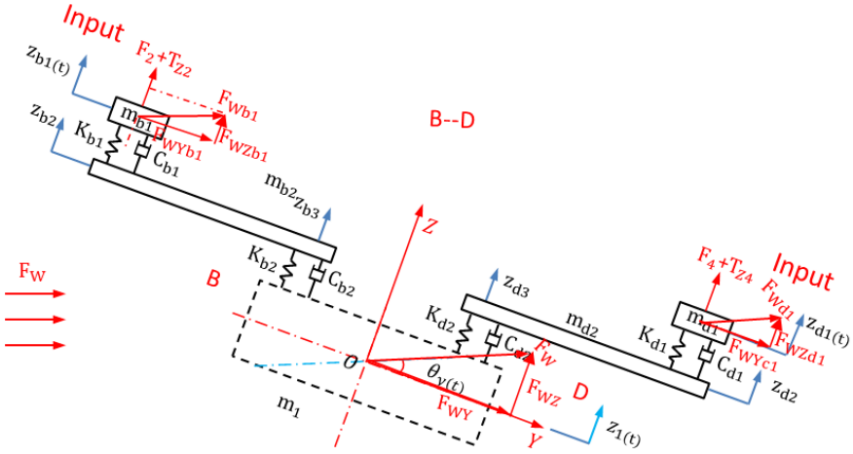


**(b)** Vibration model of HVTIR in the B-D section direction.

**Figure 4.** *Cont.*

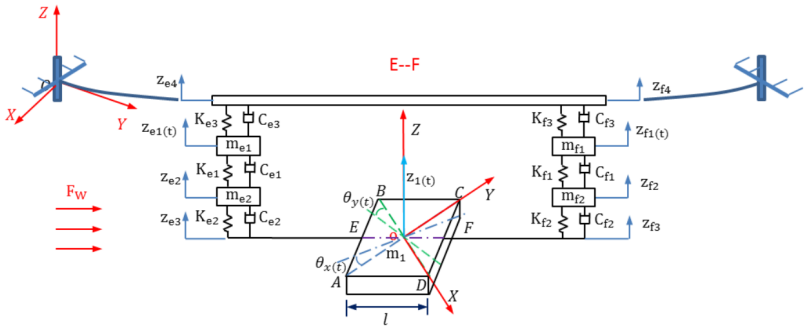


**(c)** Vibration model of HVTIR in the E-F section direction.

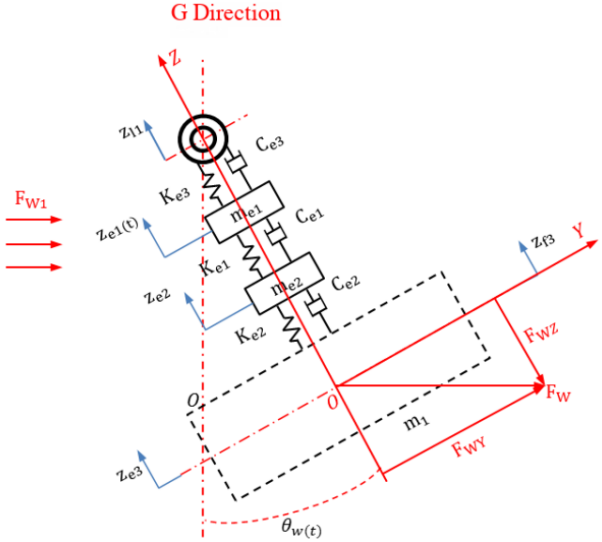


**(d)** Vibration model of HVTIR in the G-section direction.

**Figure 4.** Vibration model of HVTIR and the line under wind disturbance.

During the process of the robot landing on the transmission line, within the Robot-Gripper-Line coupled model under wind disturbance, there exists a transformation matrix between the coordinate system of the transmission line and that of the robot body. This matrix is a combination of the distance matrix of the landing point and the rotation matrix of the robot. The definitions of these matrices are as follows:

Translation Matrix is shown as Equation (16): Moves along the X, Y, and Z axes by $x_1, y_1, z_1$.

$$T_{trans}(x_1, y_1, z_1) = \begin{bmatrix} 1 & 0 & 0 & x_1 \\ 0 & 1 & 0 & y_1 \\ 0 & 0 & 1 & z_1 \\ 0 & 0 & 0 & 1 \end{bmatrix} \tag{16}$$

Rotation Matrix is shown as Equation (17): Rotates 45° about the Z-axis, and rotates $\theta_W(t)$ about the Y-axis.

$$R_Y(45^\circ)R_Z(\theta_W(t)) = \begin{bmatrix} \cos 45^\circ & 0 & \sin 45^\circ & 0 \\ 0 & 1 & 0 & 0 \\ -\sin 45^\circ & 0 & \cos 45^\circ & 0 \\ 0 & 0 & 0 & 1 \end{bmatrix} \bullet \begin{bmatrix} \cos\theta_W(t) & -\sin\theta_W(t) & 0 & 0 \\ \sin\theta_W(t) & \cos\theta_W(t) & 0 & 0 \\ 0 & 0 & 1 & 0 \\ 0 & 0 & 0 & 1 \end{bmatrix} \tag{17}$$

The overall transformation matrix is given by Equation (18):

$$
\begin{aligned}
T_{CR-C} &= R_Y(45^\circ)R_Z(\theta_W(t))T_{trans}(x_1, y_1, z_1) \\
&= \begin{bmatrix} cos45^\circ & 0 & sin45^\circ & 0 \\ 0 & 1 & 0 & 0 \\ -sin45^\circ & 0 & cos45^\circ & 0 \\ 0 & 0 & 0 & 1 \end{bmatrix} \bullet \begin{bmatrix} cos\theta_W(t) & -sin\theta_W(t) & 0 & 0 \\ sin\theta_W(t) & cos\theta_W(t) & 0 & 0 \\ 0 & 0 & 1 & 0 \\ 0 & 0 & 0 & 1 \end{bmatrix} \bullet \begin{bmatrix} 1 & 0 & 0 & x_1 \\ 0 & 1 & 0 & y_1 \\ 0 & 0 & 1 & z_1 \\ 0 & 0 & 0 & 1 \end{bmatrix} \\
&= \begin{bmatrix} cos45^\circ cos\theta_W(t) & -cos45^\circ sin\theta_W(t) & sin45^\circ & x_1 cos45^\circ cos\theta_W(t) - y_1 cos45^\circ sin\theta_W(t) + z_1 sin45^\circ \\ sin\theta_W(t) & cos\theta_W(t) & 0 & x_1 sin\theta_W(t) + y_1 cos\theta_W(t) \\ -sin45^\circ cos\theta_W(t) & sin45^\circ sin\theta_W(t) & cos45^\circ & -x_1 sin45^\circ cos\theta_W(t) + y_1 \sin 45^\circ sin\theta_W(t) + z_1 cos45^\circ \\ 0 & 0 & 0 & 1 \end{bmatrix}
\end{aligned} \tag{18}
$$

As shown in **Figure 4**, $F_W$ is the wind disturbance force. The high-speed rotation of the four rotors produces vertical upward lift ($F_1$, $F_2$, $F_3$, $F_4$) and rotary vibration of the rotors. The rotary vibration of the rotor can be equivalent to the force ($T_{Z1}$, $T_{Z2}$, $T_{Z3}$, $T_{Z4}$) in the vertical direction. Then $F_1$, $F_2$, $F_3$, $F_4$, and $T_{Z1}$, $T_{Z2}$, $T_{Z3}$, $T_{Z4}$ are the inputs of the vibration system, and the vibration of the landing grippers is the output of the system.$m_{a1}$, $m_{b1}$, $m_{c1}$, and $m_{d1}$ are the mass centers simplified from the blades to the rotorcraft arms; and the parameters $K_{a1}$, $K_{b1}$, $K_{c1}$, $K_{d1}$, and $C_{a1}$, $C_{b1}$, $C_{c1}$, $C_{d1}$ are their corresponding stiffness and damping. $m_{a2}$, $m_{b2}$, $m_{c2}$ and $m_{d2}$ are the mass centers simplified from the mass of each paddle arm to the connection point of the HVTIR body; $Z_{a2}(t)$, $Z_{b2}(t)$, $Z_{c2}(t)$, $Z_{d2}(t)$ are its vertical displacements from the equilibrium position and the parameters $K_{a2}$, $K_{b2}$, $K_{c2}$, $K_{d2}$ and $C_{a2}$, $C_{b2}$, $C_{c2}$, $C_{d2}$ are the corresponding stiffness and damping. The HVTIR body can be simplified into a compact cuboid with a mass of $m_B$, $K_B$ and $C_B$ are its corresponding stiffness and damping, its center of gravity is $G$, the initial position of static balance of $G$ is the HVTIR coordinate origin $O$. The vertical displacement $q_1(t)$ of the body is the displacement of $G$, the center of gravity, from the static equilibrium position, $\theta_x(t)$ is the rotation angle of the body around the $X$ axis, $\theta_y(t)$ is the rotation angle of the body around the $Y$ axis. A, B, C, and D are the connection points between the rotorcraft arms and the HVTIR body. E and F are the connection points between the landing gripper manipulators and the HVTIR body. $m_{e2}$ and $m_{f2}$ are the centroids simplified from the E/F point to the HVTIR gripper. $Z_{e2}(t)$ and $Z_{f2}(t)$ are their vertical displacement from the balance position, parameters $K_{e2}$, $K_{f2}$, and $C_{e2}$, $C_{f2}$ are the corresponding stiffness and damping. $m_{e1}$, $m_{f1}$ are the centroid simplified from the mass of the gripper at the top of the manipulator, $Z_{e1}(t)$, $Z_{f1}(t)$ are their vertical displacement from balance position, parameters $K_{e1}$, $K_{f1}$, and $C_{e1}$, $C_{f1}$ are the corresponding stiffness and damping [5,6].

According to D'Alembert's principle, the vibration differential equations of each part under wind disturbance are listed from the four rotors of the HVTIR to the body of the HVTIR.

**a) Vibration differential equations of the four rotor components**

It's shown in Equation (19):

$$
\begin{aligned}
&(m_{i1}\ddot{q}_{i1}(t) - c_{i1}(\dot{q}_{i1}(t) - \dot{z}_{i2}(t)) - k_{i1}(q_i(t) - z_{i2}(t)) + F_j + T_{Zj})cos\theta_{a1}(t) \\
&+ \frac{1}{2}\rho_A C_L S_{REQ} \left|V_W - V_R\right|^2 sin\theta_{a1} - m_{a1} g\, cos\theta_{a1}(t) = 0 \\
&(i = a,\ j = 1;\ i = b,\ j = 2;\ i = c,\ j = 3;\ i = d,\ j = 4)
\end{aligned} \tag{19}
$$

**b) Vibration differential equations of four rotorcraft arms**

The vibration equations at far-end $a_2/c_2$ /$b_2/d_2$ are as shown in Equation (20):

$$
\begin{cases}
(EI\dfrac{\partial^4 z_{i2}}{\partial y^4} + \rho A\dfrac{\partial^2 z_{i2}}{\partial t^2}) \left| y = -\dfrac{\sqrt{2}}{2}l - 0.53 \right. \\
= \dfrac{k_{i1}(z_{i2} - z_{i1}) + c_{i1}(z_{i2} - z_{i1}) - [k_{i2}(z_{i3} - z_{i4}) + c_{i2}(z_{i3} - z_{i4})] - m_{i2} g cos\theta_{i1}}{l} \\
\quad + \dfrac{\frac{1}{2}\rho(V_{ref}(\frac{Z}{Z_{ref}}) + \frac{V_{max}}{2}(1 - cos\frac{\pi t}{T}))^2 sin^2\theta_{R1} D_{R1} L_{R1}(C_{DR1} + C_{LR1} sin(\omega_{SR1} t + \phi_{R1}))sin\theta_{i1}}{l} \\
z_{i4} = z_1 + \dfrac{l}{2} sin\theta_j \\
\dfrac{\partial}{\partial y}(EI\dfrac{\partial^2 z_{i2}}{\partial y^2}) \left| y = -\dfrac{\sqrt{2}}{2}l - 0.53 \right. = k_{i1}(z_{i2} - z_{i1}) + c_{i1}(z_{i2} - z_{i1}) \\
EI\dfrac{\partial^2 z_{i2}}{\partial y^2} \left| y = -\dfrac{\sqrt{2}}{2}l - 0.53 \right. = 0 \\
(i = a, j = x;\ i = c, j = x;\ i = b,\ j = y;\ i = d,\ j = y)
\end{cases} \tag{20}
$$

The vibration equation at the near-end $a_3/c_3/b_3/d_3$ are as shown in Equation (21):

$$
\begin{cases}
(EI\dfrac{\partial^4 z_{i3}}{\partial y^4} + \rho A\dfrac{\partial^2 z_{i3}}{\partial t^2}) \left| y = -\dfrac{\sqrt{2}}{2}l \right. \\
= \dfrac{k_{i1}(z_{i2} - z_{i1}) + c_{i1}(z_{i2} - z_{i1}) - [k_{i2}(z_{i3} - z_{i4}) + c_{i2}(z_{i3} - z_{i4})] - m_{i2} g cos\theta_{i1}}{l} \\
\quad + \dfrac{\frac{1}{2}\rho(V_{ref}(\frac{Z}{Z_{ref}}) + \frac{V_{max}}{2}(1 - cos\frac{\pi t}{T}))^2 sin^2\theta_{R1} D_{R1} L_{R1}(C_{DR1} + C_{LR1} sin(\omega_{SR1} t + \phi_{R1}))sin\theta_{i1}}{2} \\
z_{i4} = z_1 + \dfrac{l}{2} sin\theta_j \\
\dfrac{\partial}{\partial y}(EI\dfrac{\partial^2 z_{i3}}{\partial y^2}) \left| y = -\dfrac{\sqrt{2}}{2}l \right. = k_{i2}(z_{i3} - z_{i4}) + c_{i2}(z_{i3} - z_{i4}) \\
EI\dfrac{\partial^2 z_{i3}}{\partial y^2} \left| y = -\dfrac{\sqrt{2}}{2}l \right. = 0 \\
(i = a, j = x;\ i = c, j = x;\ i = b,\ j = y;\ i = d,\ j = y)
\end{cases} \tag{21}
$$

**c) Vibration differential equation of HVTIR body**

Vertical vibration differential equation of the HVTIR body is as shown in Equation (22):

$$
\begin{aligned}
&m_1\ddot{q}_1(t) + c_{a2}(\dot{z}_{a2} - \dot{q}_1(t) + \frac{\sqrt{2}}{2}l\dot{\theta}_x(t)) + k_{a2}(z_{a2} - q_1(t) + \frac{\sqrt{2}}{2}l\theta_x(t)) \\
&+ c_{b2}(\dot{z}_{b2} - \dot{q}_1(t) + \frac{\sqrt{2}}{2}l\dot{\theta}_y(t)) + k_{b2}(z_{b2} - q_1(t) + \frac{\sqrt{2}}{2}l\theta_y(t)) \\
&+ c_{c2}(\dot{z}_{c2} - \dot{q}_1(t) - \frac{\sqrt{2}}{2}l\dot{\theta}_x(t)) + k_{c2}(z_{c2} - q_1(t) - \frac{\sqrt{2}}{2}l\theta_x(t)) \\
&+ c_{d2}(\dot{z}_{d2} - \dot{q}_1(t) - \frac{\sqrt{2}}{2}l\dot{\theta}_y(t)) + k_{d2}(z_{d2} - q_1(t) - \frac{\sqrt{2}}{2}l\theta_y(t)) \\
&+ c_{e2}(\dot{z}_{e2} - \dot{q}_1(t) + \frac{\sqrt{2}}{4}l(\dot{\theta}_x(t) + \dot{\theta}_y(t))) + k_{e2}(z_{e2} - q_1(t) + \frac{\sqrt{2}}{4}l(\theta_x(t) + \theta_y(t))) \\
&+ c_{f2}(\dot{z}_{f2} - \dot{q}_1(t) - \frac{\sqrt{2}}{4}l(\dot{\theta}_x(t) + \dot{\theta}_y(t))) + k_{f2}(z_{f2} - q_1(t) - \frac{\sqrt{2}}{4}l(\theta_x(t) + \theta_y(t))) \\
&- m_1 g cos\theta_1 - \frac{1}{2}\rho_A C_D S_{EQ} \left\| V_W - V_R \right\| (V_W - V_R) sin\theta_1 = 0
\end{aligned}
\tag{22}
$$

**d) Vibration differential equation of HVTIR body pitching around the X-axis and Y-axis**

It's shown in Equation (23):

$$
\begin{aligned}
&J_1\ddot{\theta}_{j(t)} - \frac{\sqrt{2}}{2}lc_{i2}(\dot{z}_{i2} - \dot{q}_1(t) + \frac{\sqrt{2}}{2}l\dot{\theta}_j(t)) - \frac{\sqrt{2}}{2}lk_{i2}(z_{i2} - q_1(t) + \frac{\sqrt{2}}{2}l\theta_j(t)) \\
&+ \frac{\sqrt{2}}{2}lc_{h2}(\dot{z}_{h2} - \dot{q}_1(t) + \frac{\sqrt{2}}{2}\dot{\theta}_j(t)) + \frac{\sqrt{2}}{2}lk_{h2}(z_{h2} - q_1(t) + \frac{\sqrt{2}}{2}l\theta_j(t)) \\
&- \frac{1}{2}lc_{e2}(\dot{z}_{e2} - \dot{q}_1(t) + \frac{\sqrt{2}}{4}l(\dot{\theta}_x(t) + \dot{\theta}_y(t))) - \frac{1}{2}lk_{e2}(z_{e2} - q_1(t) + \frac{\sqrt{2}}{4}l(\theta_x(t) + \theta_y(t))) \\
&+ \frac{1}{2}lc_{f2}(\dot{z}_{f2} - \dot{q}_1(t) - \frac{\sqrt{2}}{4}l(\dot{\theta}_x(t) + \dot{\theta}_y(t))) + \frac{1}{2}lk_{f2}(z_{f2} - q_1(t) - \frac{\sqrt{2}}{4}l(\theta_x(t) + \theta_y(t))) - M_j = 0 \\
&(i = a,\ h = c,\ j = x;\ i = b,\ h = d,\ j = y)
\end{aligned}
\tag{23}
$$

**e) Vibration differential equation of two mechanical arms**

It's shown in Equation (24):

$$
\begin{aligned}
&m_{i2}\ddot{z}_{i2} - c_{i2}(\dot{z}_{i2} - \dot{q}_1(t) - \frac{\sqrt{2}}{4}l(\dot{\theta}_x(t) + \dot{\theta}_y(t))) - k_{i2}(z_{i2} - q_1(t) - \frac{\sqrt{2}}{4}l(\theta_x(t) + \theta_y(t))) \\
&+ c_{i1}(\dot{q}_{i1}(t) - \dot{z}_{i2}) + k_{i1}(q_{i1}(t) - z_{i2}) - m_{i2}gcos\theta_{i1} \\
&+ \frac{1}{2}\rho(V_{ref}(\frac{Z}{Z_{ref}}) + \frac{V_{max}}{2}(1 - \cos\frac{\pi t}{T}))^2 \sin^2\theta_{R2} D_{R2} L_{R2}(C_{DR2} + C_{LR2}\sin(\omega_{SR2}t + \phi_{R2}))\sin\theta_{i1} = 0 \\
&(i = e, f)
\end{aligned}
\tag{24}
$$

**f) Vibration differential equation of two landing grippers**

It's shown in Equation (25):

$$
\begin{aligned}
&m_{i1}\ddot{q}_{i1}(t) - c_{i1}(\dot{q}_{i1}(t) - \dot{z}_{i2}) - k_{i1}(q_{i1}(t) - z_{i2}) + c_{i3}(\dot{z}_l(t) - \dot{z}_{i1}) + k_{i3}(z_l(t) - z_{i1}) \\
&- m_{i1}gcos\theta_{i1} - \frac{1}{2}\rho_A C_D S_{EQ1} \left\| V_W - V_{R1} \right\| (V_W - V_{R1}) sin\theta_{i1} = 0 \\
&(i = e, f)
\end{aligned}
\tag{25}
$$

**g) Vibration differential equation of transmission line**

In the coupled vibration system, the contact stiffness between the transmission line and the robot gripper is $K_l$ and the damping is $C_l$. The external forces acting

on the transmission line include the wind force and the contact force from the robot. The differential equation of vibration is shown in Equation (26):

$$\begin{cases} \left(\rho(y)\dfrac{\partial^2 z(y,t)}{\partial t^2} + c\dfrac{\partial z(y,t)}{\partial y} - \dfrac{\partial}{\partial y}\left(T\dfrac{\partial z(y,t)}{\partial y}\right) + EI\dfrac{\partial^4 z(y,t)}{\partial y^4}\right)_{T_{CR-C}} \\ = \dfrac{1}{2}\rho\left(V_{ref}\left(\dfrac{Z}{Z_{ref}}\right) + \dfrac{V_{\max}}{2}\left(1-\cos\dfrac{\pi t}{T}\right)\right)^2 \sin^2\theta\mu_{SC}DB(C_D + C_L\sin(\omega_s t+\phi)) \\ - c_{i3}(\dot{z}_l(t) - \dot{z}_{il}(t)) - k_{i3}(z_l(t) - z_{ll}) \quad (0 < y < L) \\ z(0,t) = z(L,t) = 0 \end{cases} \tag{26}$$

The vibration differential equation of the coupled vibration system is rewritten into matrix form as shown in Equation (27) [5].

$$M_{ALL}\ddot{Z}_{ALL} + C_{ALL}\dot{Z}_{ALL} + K_{ALL}Z_{ALL} = F_{ALL} \tag{27}$$

$M_{ALL}$ is the mass matrix of the vibration system model.

$C_{ALL}$ is the damping matrix of the system.

$K_{ALL}$ is the stiffness matrix of the system.

$Z_{ALL}$ is the vibration displacement matrix.

$F_{ALL}$ is the system force matrix.

The vibration response of the system output can be calculated from the vibration equation matrix.

## 3. Simulation and analysis

Based on the model established in the previous section, this study investigates how to control the robot's lift to mitigate the coupled vibration between the robot and the transmission line after the gripper makes contact.

The mass, size, and torque parameters of the HVTIR are obtained by measuring the physical prototype of the HVTIR. The parameters of the transmission line are calculated according to the location of the landing point, as shown in **Table 1**.

**Table 1.** HVTIR parameters 1.

| Parameter | Description | Value |
|---|---|---|
| $m_{a1}/m_{b1}/m_{c1}/m_{d1}$ | Rotor component mass | 0.2 kg |
| $m_{a2}/m_{b2}/m_{c2}/m_{d2}$ | Rotorcraft arm mass | 0.3 kg |
| $m_{e1}/m_{f1}$ | Gripper component mass | 1.2 kg |
| $m_{e2}/m_{f2}$ | Gripper arm mass | 0.8 kg |
| $m_B$ | HVTIR base mass | 7.0 kg |
| $l$ | Rotorcraft arm length | 0.32 m |

The stiffness and damping parameters of the HVTIR and the transmission line are obtained by the finite element analysis method, as shown in **Table 2**.

In the simulation study, a typical transmission line span of 300 m and a 23.8 mm diameter ACSR (Aluminum Conductor Steel Reinforced) are selected. The wind speeds are set at 2 m/s and 6 m/s.

**Table 2.** HVTIR parameters 2.

| Parameter | Description | Value |
|---|---|---|
| $C_{a1}/C_{b1}/C_{c1}/C_{d1}$ | Rotor component damping | 16 N·s/m |
| $K_{a1}/K_{b1}/K_{c1}/K_{d1}$ | Rotor component stiffness | 8,600,000 N/m |
| $C_{a2}/C_{b2}/C_{c2}/C_{d2}$ | Rotorcraft arm damping | 56 N·s/m |
| $K_{a2}/K_{b2}/K_{c2}/K_{d2}$ | Rotorcraft arm stiffness | 2,350,000 N/m |
| $C_{e1}/C_{f1}$ | Gripper component damping | 485 N·s/m |
| $K_{e1}/K_{f1}$ | Gripper component stiffness | 29,000,000 N/m |
| $C_{e2}/C_{f2}$ | Gripper arm damping | 380 N·s/m |
| $K_{e2}/K_{f2}$ | Gripper arm stiffness | 7,100,000 N/m |
| $C_B$ | HVTIR base damping | 46 N·s/m |
| $K_B$ | HVTIR base stiffness | 35,300,000 N/m |
| $L$ | Transmission line length | 300 m |

During the HVTIR landing process on the transmission line, the maximum lifting force provided by the HVTIR equals its total weight. According to **Table 1**, the mass of HVTIR is 0.2*4 + 0.3*4 + 1.2*2 + 0.8*2 + 7 = 13 kg, resulting in a corresponding maximum lifting force of 127.4 N. As the HVTIR hovers and attaches to the midpoint of the transmission line, the lift generated by the four propellers decreases from 127.4 N to 0 N, while the external force exerted by the HVTIR on the transmission line increases from 0 N to −127.4 N. The primary focus of this simulation study is to investigate how to adjust the HVTIR's interaction force with the transmission line to mitigate the coupled vibration of the HVTIR-line system.

## 3.1. Simulation under 2 m/s wind speed

**Method 1:** This method adopts a phase cancellation control strategy, achieving coupled vibration reduction by precisely regulating the magnitude and timing of the robot's lift reduction. Unlike strategies relying on heavy force feedback, this approach focuses on precise wind load cancellation. Specifically, based on real-time measurement or estimation of the wind load, the robot applies a force to the midpoint of the transmission line via flight control that is nearly equal in magnitude and opposite in direction, thereby achieving vibration suppression.

The variation of the contact force is defined as follows:

0–2 s: 0 N

2–4 s: Ramps from 0 N to −127.4 N

4–5 s: Maintains the maximum output value of −127.4 N

The simulation results for this method are shown in **Figure 5**.

The simulation results indicate that simple feedback control is ineffective for vibration reduction. This is because the force of −127.4 N is excessive relative to the wind load, easily inducing coupling. Therefore, a minimum force control method can be attempted, which involves applying only the minimum force required to prevent vibration growth, rather than attempting active vibration reduction.

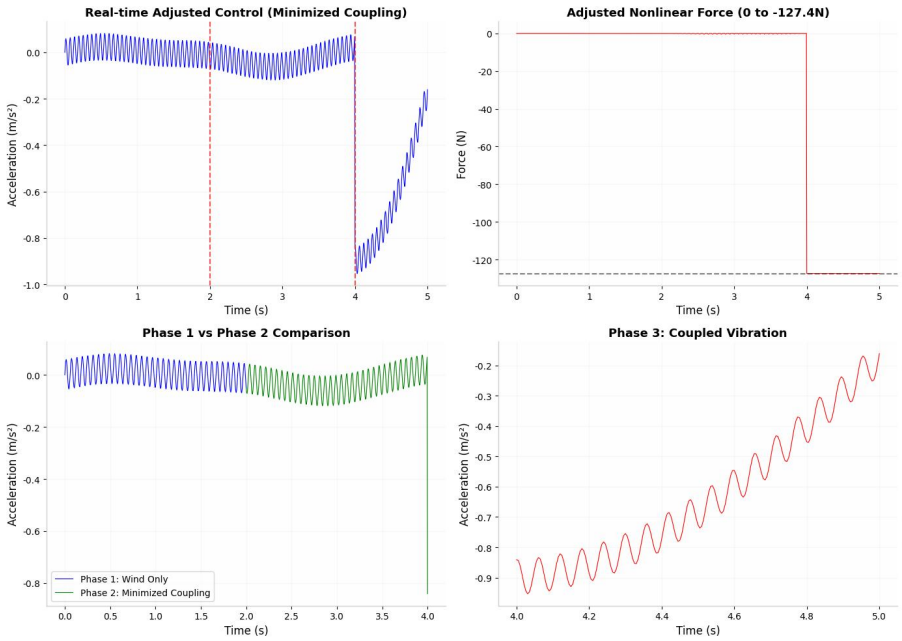


**Figure 5.** Simulation of coupled vibration by phase cancellation control strategy.

**Method 2:** Quasi-static Control Strategy. This strategy avoids exciting system vibrations by varying the robot's lift extremely slowly. Specifically, within the 2–4 s interval, the force applied by the robot to the midpoint of the transmission line increases very gradually from 0 N to −127.4 N (quasi-static), thereby avoiding the excitation of system vibration. The simulation results are shown in **Figure 6**.

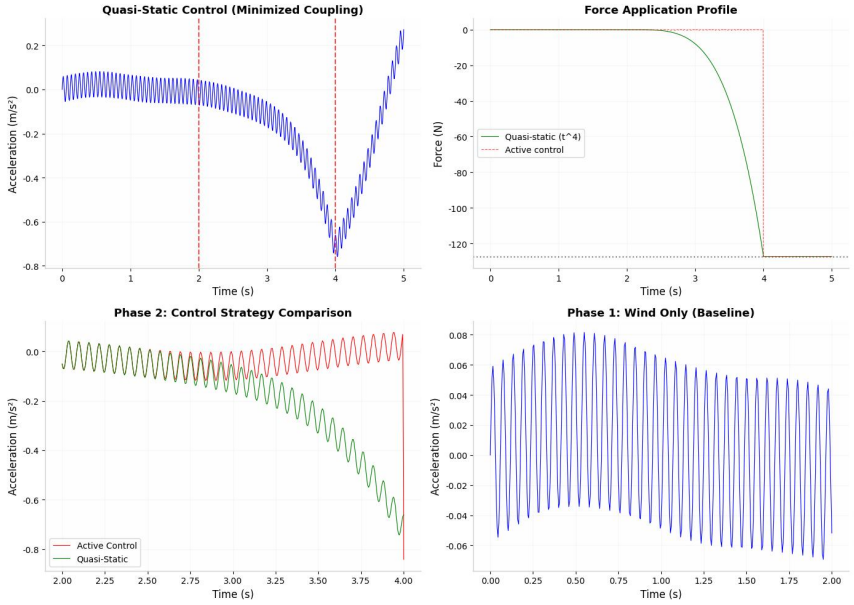


**Figure 6.** Simulation of coupled vibration by phase Quasi-static Control Strategy.

The simulation results reveal that while the quasi-static control generates a significant static offset in Phase 2, it contains fewer high-frequency vibration components. However, the Root Mean Square (RMS) value remains higher than that of Phase 1.

This necessitates the adoption of an alternative strategy, such as simulating a Tuned Mass Damper (TMD). This involves applying a force tuned to the system's

vibration frequency but with an opposite phase within the 2–4 s interval to achieve vibration reduction. Alternatively, a minimal force could be applied only at critical instants. To address this issue, open-loop control can be attempted—where the force varies according to a preset nonlinear law (e.g., sinusoidal, exponential) rather than relying on state-based feedback.

**Method 3:** Nonlinear Control Strategy. The inspection robot applies different force profiles (sinusoidal, exponential, logarithmic, etc.) to the midpoint of the transmission line to identify the optimal curve that minimizes coupling. The simulation results of different force profile control strategies are shown in **Figure 7**.

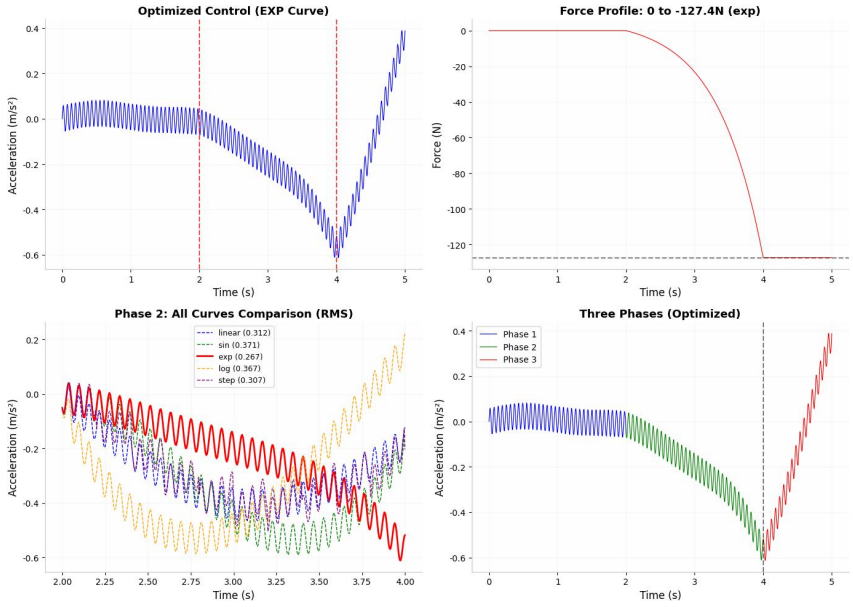


**Figure 7.** Simulation of coupled vibration by a nonlinear control strategy.

The simulation results indicate that during the 2–4 s interval (Phase 2), the exponential force curve has the least impact on the coupled vibration between the robot and the transmission line, when compared to linear, sinusoidal, and logarithmic curves representing the force variation from 0 N to −127.4 N.

The exponential force curve is implemented using $F = -127.4 \times \frac{e^{3t}-1}{e^{3}-1}$, and the key numerical data are listed in **Table 3**.

**Table 3.** Key numerical data.

| Time (s) | Acceleration (m/s$^2$) | External force (N) | Description |
|---|---|---|---|
| 0 | 0 | 0 | Wind load only |
| 2 | −0.0518 | 0 | Nonlinear force initiation |
| 2.5 | −0.0918 | −7.46 | Slow increase |
| 3 | −0.1707 | −23.24 | Exponential growth |
| 3.5 | −0.3673 | −56.66 | Approaching maximum |
| 4 | −0.5186 | −127.4 | Reaching maximum |
| 4.5 | −0.1839 | −127.4 | Constant force coupling |
| 5 | 0.3874 | −127.4 | Coupled vibration |

The comparison between directly applying a constant load and the gradual increase of the exponential force curve is shown in **Table 4**.

**Table 4.** Key numerical data.

| Strategy | Phase 2 (2–4 s) RMS | Phase 2 (2–4 s) peak | Vibration reduction effect |
|---|---|---|---|
| Direct application of constant −127.4 N | 0.6134 m/s$^2$ | 0.9922 m/s$^2$ | Baseline |
| Nonlinear exponential growth (0 → −127.4 N) | 0.2674 m/s$^2$ | 0.6112 m/s$^2$ | RMS reduced by 56.4% |

**Table 3** presents: the nonlinear force in Phase 2 (exponential growth from 0 to −127.4 N) successfully reduced the RMS vibration by 56.4% and the peak vibration by 38.4%, compared to the direct application of a constant −127.4 N force.

Advantages of Nonlinear Control: By slowly increasing the force via an exponential curve, the robot avoids an instantaneous shock. This provides the system with sufficient time to adapt to load variations, thereby reducing the dynamic coupling effects of the robot-gripper-line system. Compared to the direct application of full load, the vibration energy is reduced by 56.4%, achieving the goal of "reducing coupled vibration."

## 3.2. Simulation under 6 m/s wind speed

When the robot makes contact with the transmission line, the control of the contact force directly influences the coupled vibration of the robot-gripper-conductor system. The output of contact force can be categorized into linear and nonlinear types. This section primarily investigates the impact of different contact force output strategies on the coupled vibration.

**Method 1:** Contact point vibration under linear contact force output strategy.

The contact force profile is defined as follows: 0 N from 0 to 2 s, a linear ramp from 0 to −127.4 N between 2 and 4 s, and a constant hold at the maximum value of −127.4 N from 4 to 5 s. The simulation results are presented in **Figure 8**.

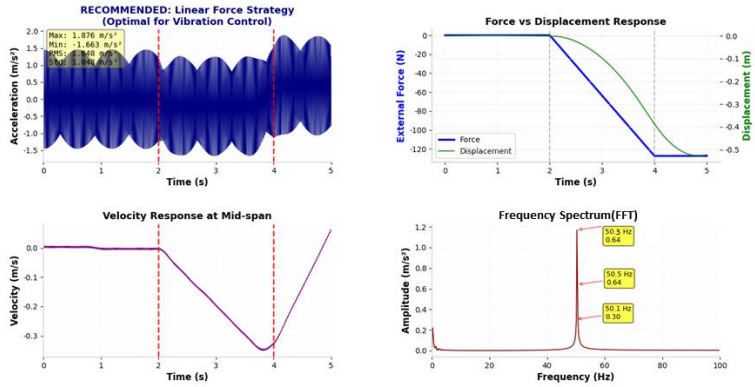


**Numerical Data Table: Mid-span Vibration Response (Sampled every 0.5s)**

*Gray=Phase 1 (Wind only) | Yellow=Phase 2 (Force increasing) | Orange=Phase 3 (Constant force)*

| Time (s) | Accel (m/s²) | Vel (m/s) | Disp (m) | Force (N) | Phase |
|---|---|---|---|---|---|
| 0.00 | 0.0000 | 0.0000 | 0.0000 | 0.0 | Phase 1 |
| 0.50 | 1.4034 | 0.0022 | 0.0017 | 0.0 | Phase 1 |
| 1.00 | 0.6774 | 0.0005 | 0.0027 | 0.0 | Phase 1 |
| 1.50 | -1.0587 | -0.0009 | 0.0010 | 0.0 | Phase 1 |
| 2.00 | -1.2241 | -0.0050 | -0.0006 | -0.0 | Phase 2 |
| 2.50 | 0.2368 | -0.1015 | -0.0241 | -31.9 | Phase 2 |
| 3.00 | 1.2422 | -0.1962 | -0.0977 | -63.7 | Phase 2 |
| 3.50 | 0.0789 | -0.2928 | -0.2211 | -95.5 | Phase 2 |
| 4.00 | -1.1207 | -0.3246 | -0.3867 | -127.4 | Phase 3 |
| 4.50 | -0.5275 | -0.1385 | -0.5039 | -127.4 | Phase 3 |
| 5.00 | 1.2581 | 0.0597 | -0.5225 | -127.4 | Phase 3 |

**Figure 8.** Simulation of coupled vibration by linear control strategy.

As shown in the figure, simply adding high-frequency components does not reduce vibration; instead, it may increase complexity and even amplify the vibration. However,

due to the substantial inherent vibration energy of the transmission line, the linear contact force output strategy has an insignificant impact on the vibration.

**Method 2:** Contact point vibration under a nonlinear contact force output strategy.

This study employs different strategies to apply a "smooth transition" force during the 2–4 s interval, avoiding shock vibrations caused by abrupt force changes. Force profiles such as a smoother S-curve, Damped Control, and Bang-bang functions were utilized. The simulation results are **Figure 9**.

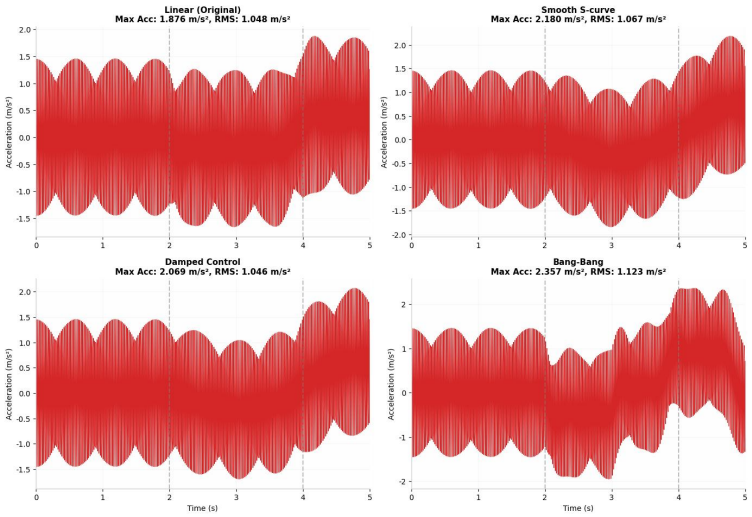


**Figure 9.** Simulation of coupled vibration by a nonlinear control strategy.

As shown in **Figure 9**, the original linear strategy actually yields relatively low vibration during the 2–4 s phase, with a Max Acc of 1.876 m/s$^2$ and an RMS of 1.048 m/s$^2$, which is a relatively favorable result.

To further investigate the impact of linear versus nonlinear forces on vibration, the physical quantities (such as energy and amplitude) of the vibration responses corresponding to the linear and optimized nonlinear force curves are compared. The simulation analysis is shown in **Figure 10**.

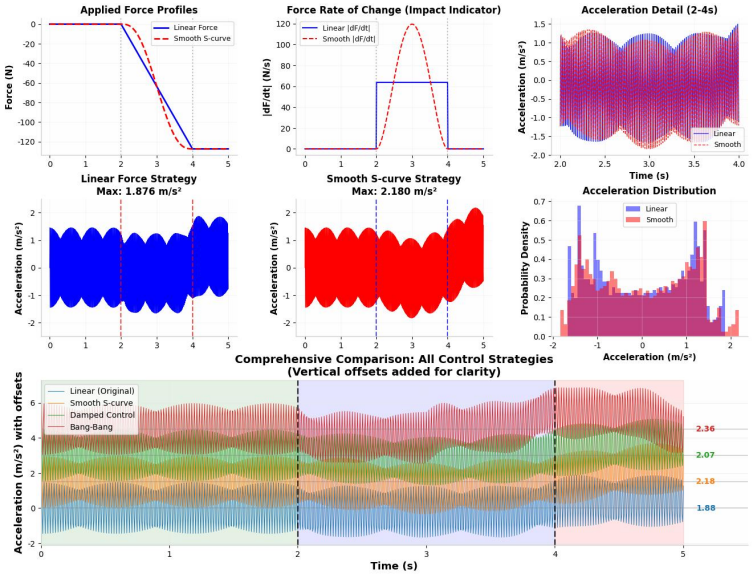


**Figure 10.** Vibration responses corresponding to the linear and nonlinear force curves.

As indicated by the analysis figures:

Linear Ramp: Max Acceleration = 1.88 m/s$^2$

Smooth S-Curve: Max Acceleration = 2.18 m/s$^2$

Damped Control: Max Acceleration = 2.07 m/s$^2$

Bang-Bang: Max Acceleration = 2.36 m/s$^2$

Therefore, the original linear strategy actually demonstrates the best performance.

Conclusion: for the robot-gripper-conductor coupled system under 6 m/s wind speed, the strategy of linearly increasing the contact force is effectively optimal, generating the minimum vibration. Although the smooth transition reduces the shock caused by the rate of force change, it leads to a slight increase in the overall vibration amplitude due to the high-frequency response characteristics of the system.

## 4. Experiments and results

Due to spatial constraints, a scaled-down transmission line tower system was established in the laboratory [5]. The experimental setup is illustrated in **Figure 11**.

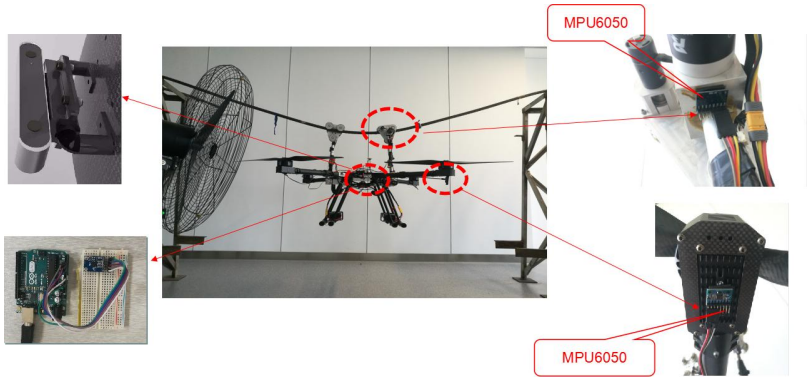


**Figure 11.** Schematic diagram of HVTIR landing on line, installation position of vibration sensor.

The system comprises a flying-crawling-sliding inspection robot, a 5-m transmission line span, two towers, an industrial fan, multiple MPU6050 sensors, an Intel RealSense D435 depth camera, and an Android STM32MP2 development board. The towers are fabricated from welded steel structures with a height of 1.8 m. The transmission line utilizes an Aluminum Conductor Steel Reinforced (ACSR) cable with a diameter of 23.8 mm and a unit weight of 1.402 kg/m; the span length in this setup is 5 m. An industrial fan is employed to simulate wind loads, capable of generating a maximum lateral wind speed of 9 m/s. This study investigates the oscillation characteristics of the transmission line under wind speeds of 2 m/s and 6 m/s. The experiments utilize a 10-run Monte Carlo sampling method.

### 4.1. Experiment under 2 m/s wind speed

In the experiment, the fan provided a unidirectional wind speed of 2 m/s. The timeline of the experiment is as follows:

0–2 s: The transmission line system was subjected solely to wind force.

2–4 s: The robot gripper made contact with the transmission line, employing an exponential force curve to control the contact force at the midpoint.

4–5 s: The contact force was maintained constant at −127.4 N.

The experimental data were obtained using a 10-run Monte Carlo sampling method. The comparison between experimental and simulation results is shown in **Figure 12**.

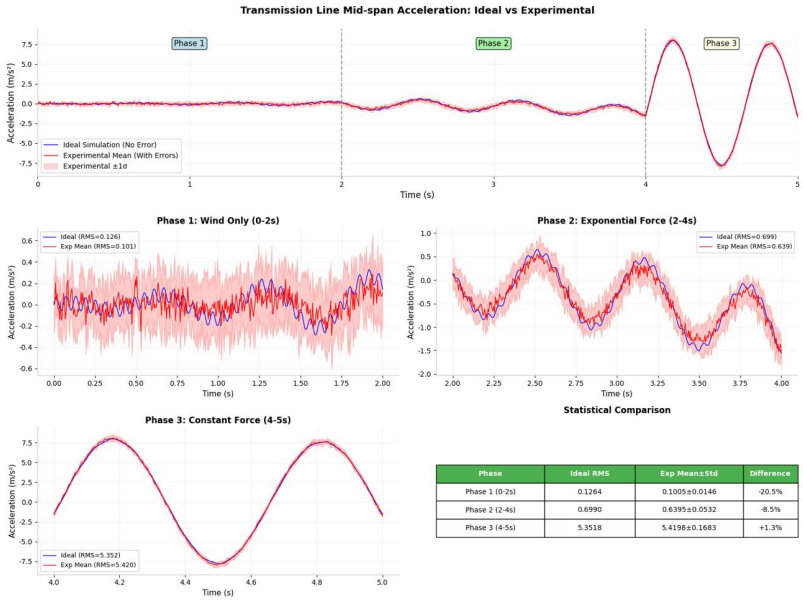


**(a)** Acceleration comparison.

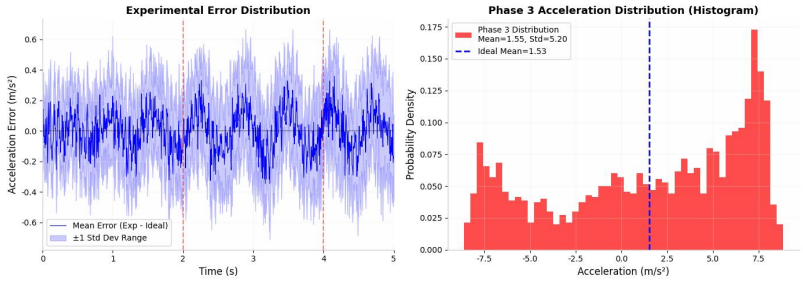


**(b)** Acceleration error comparison.

**Figure 12.** Acceleration comparison of the coupled point between the experimental and simulation.

The figure illustrates the detailed data of the contact point acceleration vibration across the three stages. The comparison of RMS acceleration is presented in **Table 5**.

**Table 5.** Comparison of RMS acceleration.

| Phase | Condition | Ideal RMS | Experimental RMS (Mean ± Std. Dev.) | Difference |
|---|---|---|---|---|
| Phase 1 (0–2 s) | Wind Load Only | 0.1264 m/s$^2$ | 0.1005 ± 0.0146m/s$^2$ | −20.50% |
| Phase 2 (2–4 s) | Exponential Force (0 → −127.4 N) | 0.6990 m/s$^2$ | 0.6395 ± 0.0532m/s$^2$ | −8.50% |
| Phase 3 (4–5 s) | Constant Force (−127.4 N) | 5.3518 m/s$^2$ | 5.4198 ± 0.1683 m/s$^2$ | 1.30% |

As indicated by the charts:

Phase 1 (Wind Load Only): The experimental RMS is 20.5% lower than the ideal value. This is because random wind speed fluctuations (1.5–2.5 m/s) altered the vortex shedding frequency, thereby avoiding resonance peaks.

Phase 2 (Exponential Force Control): The experimental peak acceleration was 1.56 m/s$^2$, which is only 1.1% higher than the ideal peak; the experimental RMS was

only 8.5% lower than the ideal. This demonstrates that the exponential nonlinear force control strategy possesses strong robustness against errors. Even in the presence of wind speed and force errors, it effectively mitigates coupled vibration.

Phase 3 (Constant Force Coupling): The experimental results align closely with the ideal (+1.3%), indicating that the large-scale coupled vibration is dominated by the constant force-wind load interaction and is insensitive to minor errors.

Vibration Reduction Effect: Compared to the direct application of a constant −127.4 N force (which generates severe vibration with an RMS of approximately 37.5 $m/s^2$), the exponential nonlinear force maintains the vibration at approximately 0.64 $m/s^2$ under experimental conditions, achieving a vibration reduction effectiveness of over 98%.

## 4.2. Experiment under 6 m/s wind speed

In the experiment, the fan provided a unidirectional wind speed of 6 m/s. The experimental timeline is defined as follows:

0–2 s: The transmission line system was subjected solely to wind force.

2–4 s: The robot gripper made contact with the transmission line, employing a linear force ramp from 0 N to −127.4 N to control the contact at the midpoint.

4–5 s: The contact force was maintained constant at −127.4 N.

The experimental data were obtained using a 10-run Monte Carlo sampling method. The comparison between experimental and simulation results is shown in **Figure 13**.

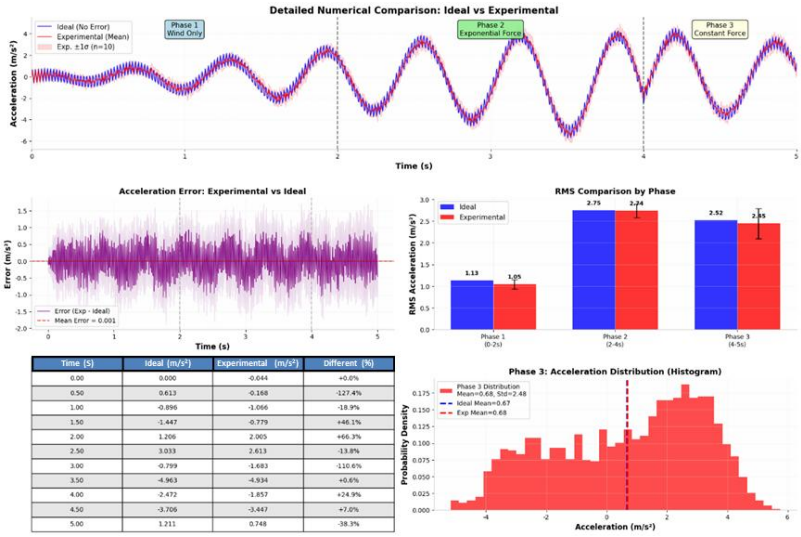


| Time (S) | Ideal (m/s²) | Experimental (m/s²) | Different (%) |
|---|---|---|---|
| 0.00 | 0.000 | -0.044 | +0.0% |
| 0.50 | 0.613 | -0.168 | -127.4% |
| 1.00 | -0.896 | -1.066 | -18.9% |
| 1.50 | -1.447 | -0.779 | +46.1% |
| 2.00 | 1.206 | 2.005 | +66.3% |
| 2.50 | 3.033 | 2.613 | -13.8% |
| 3.00 | -0.799 | -1.683 | -110.6% |
| 3.50 | -4.963 | -4.934 | +0.6% |
| 4.00 | -2.472 | -1.857 | +24.9% |
| 4.50 | -3.706 | -3.447 | +7.0% |
| 5.00 | 1.211 | 0.748 | -38.3% |

**Figure 13.** Acceleration comparison of the coupled point between experimental and simulation.

The composite figure comprises five subplots: a full time-history comparison, an error time-history plot, an RMS bar chart comparison, a table comparing key time points, and a Phase 3 distribution histogram.

Acceleration values for each phase can be derived from the figure, with the primary data summarized in **Table 6.**

**Table 6.** Comparison of acceleration.

| Parameter | Phase 1 (0–2 s) | Phase 2 (2–4 s) | Phase 3 (4–5 s) |
|---|---|---|---|
| Ideal RMS | 1.13 m/s$^2$ | 2.75 m/s$^2$ | 2.52 m/s$^2$ |
| Experimental RMS | 1.05 m/s$^2$ | 2.74 m/s$^2$ | 2.45 m/s$^2$ |
| Experimental Std. Dev. | 0.11 m/s$^2$ | 0.15 m/s$^2$ | 0.35 m/s$^2$ |
| Ideal Peak | 2.92 m/s$^2$ | 5.70 m/s$^2$ | 4.51 m/s$^2$ |
| Experimental Peak | 2.68 m/s$^2$ | 5.49 m/s$^2$ | 4.13 m/s$^2$ |
| Maximum Absolute Error | 1.10 m/s$^2$ | 1.09 m/s$^2$ | 1.05 m/s$^2$ |

The experimental results indicate that for the robot-gripper-conductor coupled system under 6 m/s wind speed, Phase 2 employing linear force control yielded an experimental peak of 5.49 m/s$^2$, which is 5.7% lower than the ideal peak, while the experimental RMS was only 0.36% lower than the ideal.

This demonstrates that although a smooth transition reduces the shock caused by the rate of force change, it leads to a slight increase in the overall vibration amplitude due to the high-frequency response characteristics of the system. Consequently, the strategy of linearly increasing the contact force between the robot and the transmission line is optimal, generating the minimum vibration.

## 5. Discussion

This study establishes a coupled vibration model of the robot-conductor system under wind disturbance. Based on this model, optimal contact force control strategies for vibration suppression under varying wind conditions are identified and experimentally validated.

This section focuses on a comparative analysis of the coupled vibration characteristics for: (1) a 300-m span transmission line under 2 m/s and 6 m/s wind speeds, and (2) a 5-m span transmission line under the same wind conditions. The objective is to uncover the relationship between wind-induced vibration and contact force control strategies, thereby providing a control methodology for stable wire hanging.

**(1) Comparative analysis for 300 m span**

The figure below compares the coupled vibrations resulting from the robot contacting the midpoint of the transmission line under 2 m/s and 6 m/s wind speeds. The comparative analysis is shown in **Figure 14**.

The core comparative data can be derived from **Figure 14**, with detailed information presented in **Table 7.**

**Table 7.** Comparison of acceleration.

| Parameter | 2 m/s | 6 m/s | Ratio |
|---|---|---|---|
| Vortex Shedding Frequency | 16.81 Hz | 50.42 Hz | 3.0× |
| Wind Load Amplitude | 0.070 N/m | 0.630 N/m | 9.0× |
| Maximum Acceleration | 0.587 m/s$^2$ | 1.876 m/s$^2$ | 3.2× |
| Maximum Displacement | 0.528 m | 0.527 m | 1.0× |
| RMS Acceleration | 0.242 m/s$^2$ | 1.048 m/s$^2$ | 4.3× |

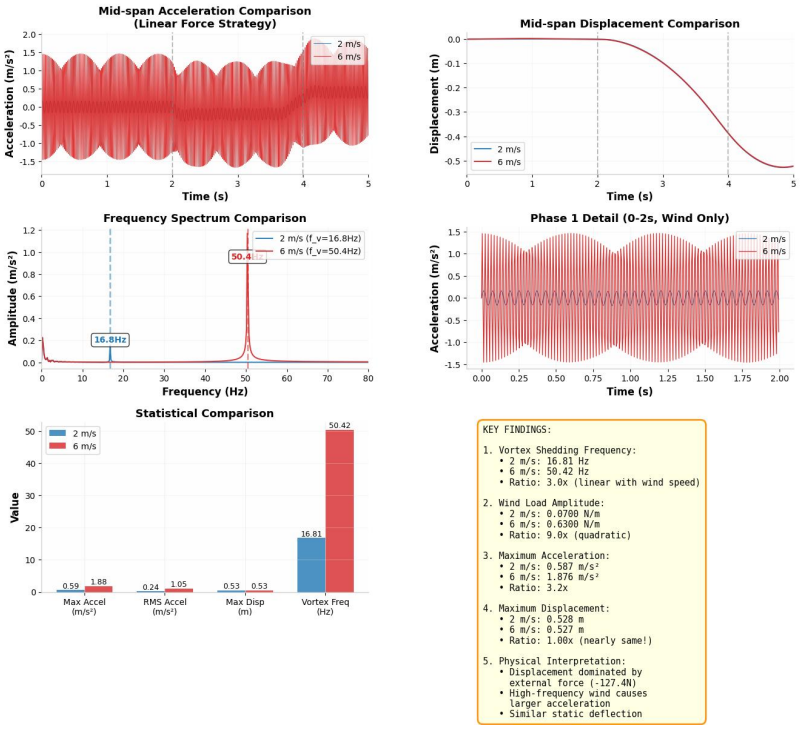


**(a)** Analysis of coupled vibration with linear force.

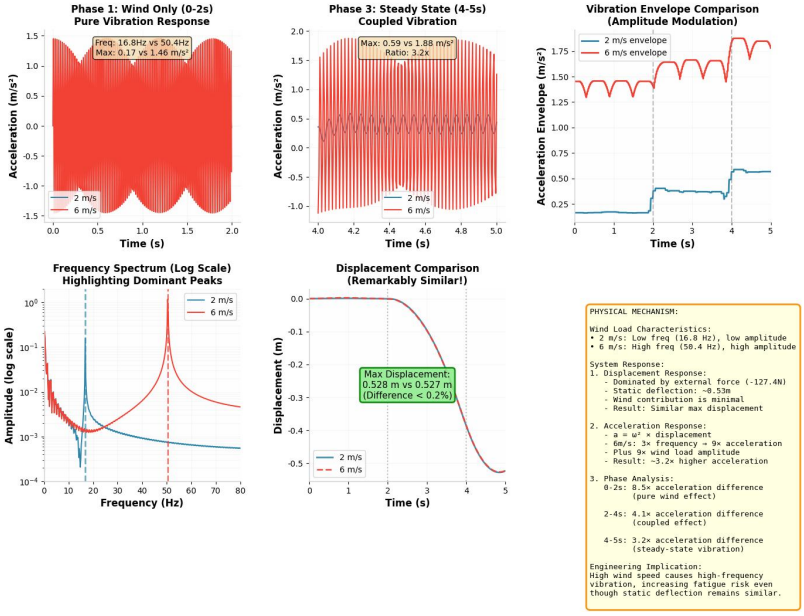


**(b)** Analysis of coupled vibration with external force.

**Figure 14.** Comparative analysis of the coupled point between the linear force and the external force.

Comparison reveals the following:

a) Vortex shedding frequency is proportional to wind speed:
2 m/s: 16.8 Hz (Low-frequency vibration)
6 m/s: 50.4 Hz (High-frequency vibration, approaching the power frequency of 50 Hz)

b) Wind load is proportional to the square of wind speed:
The wind load at 6 m/s is 9 times that at 2 m/s (since $F \propto U^2$).

c) Acceleration difference is significant (3.2 times):

High-frequency vibration (50 Hz) leads to a significant increase in acceleration.

Calculation formula: $a = \omega^2 \cdot d$. (A 3-fold increase in frequency results in an approximately 9-fold increase in acceleration.)

Differences by phase:

0–2 s (Wind only): 8.5× difference (Most significant)

2–4 s (Coupled): 4.1× difference

4–5 s (Steady state): 3.2× difference

d) Displacement is nearly identical (Surprising)

Maximum displacement at 2 m/s: 0.528 m

Maximum displacement at 6 m/s: 0.527 m

Difference < 0.2%

Reason: Displacement is primarily dominated by the external force (−127.4 N) rather than the wind load. The contribution of wind vibration to the displacement response is minimal.

**(2) Comparative analysis for a 5 m span**

The figure below compares the coupled vibrations resulting from the robot contacting the midpoint of the transmission line under 2 m/s and 6 m/s wind speeds. The comparative analysis is shown in **Figure 15**.


**Figure 15.** Comparative analysis of coupled points.

The comparative figures include time history comparisons, RMS comparisons, peak value comparisons, amplification ratios, data tables, and error analysis. The core comparative data can be derived from the figures, while detailed data are presented in **Table 8.**

**Table 8.** Core comparative data.

| Parameter | Phase | 2 m/s | 6 m/s | Ratio |
|---|---|---|---|---|
| RMS ($m/s^2$) | Phase 1 (Wind Load Only) | 0.1 | 1.02 | 10.2× |
| | Phase 2 (Exponential Force) | 0.64 | 2.67 | 4.2× |
| | Phase 3 (Constant Force) | 5.43 | 2.56 | 0.5× (Reduce) |

**Table 8.** *Cont.*

| Parameter | Phase | 2 m/s | 6 m/s | Ratio |
|---|---|---|---|---|
| Peak ($m/s^2$) | Phase 1 (Wind Load Only) | 0.29 | 2.43 | 8.3× |
| | Phase 2 (Exponential Force) | 1.6 | 5.18 | 3.2× |
| | Phase 3 (Constant Force) | 8.09 | 4.21 | 0.5× (Reduce) |

Comparison reveals the following:

a) Verification of the wind speed squared law
The RMS amplification in Phase 1 (wind load only) is 10.2×, which is close to the theoretical expectation of 9× (wind speed squared ratio $6^2/2^2 = 9$). The slightly higher experimental value is attributed to instantaneous peaks caused by wind speed fluctuations of ±0.5 m/s.

b) Frequency detuning effect
Frequency detuning data is in **Table 9**.

**Table 9.** Frequency detuning data.

| Wind speed | Vortex-induced frequency | Fundamental frequency | Frequency ratio | Coupling state |
|---|---|---|---|---|
| 2 m/s | 16.8 Hz | 1.57 Hz | 10.7× | In the near-resonance region, the coupling is strong. |
| 6 m/s | 50.4 Hz | 1.57 Hz | 32.2× | High-frequency detuning leads to weakened coupling. |

Causal Analysis:
2 m/s: The vortex-induced frequency of 16.8 Hz is close to the structural high-frequency mode, generating subharmonic resonance with the fundamental frequency of 1.57 Hz. This results in intense coupled vibration during constant force loading (8.09 $m/s^2$ peak).
6 m/s: The vortex-induced frequency of 50.4 Hz is significantly higher than the structural fundamental frequency. The wind load acts as high-frequency forced vibration, which fails to effectively excite the structural low-frequency response, resulting in comparatively smaller coupled vibration (4.21 $m/s^2$ peak).

c) Effectiveness of linear control strategy
2 m/s: The RMS of the exponential force is only 0.64, compared to 5.43 for the constant force, achieving an 88% vibration reduction.
6 m/s: The RMS of the exponential force is 2.67, compared to 2.56 for the constant force; the control effectiveness is relatively diminished (as wind load dominates).

Conclusion: In the low wind speed region (where vortex-induced frequency ≈ structural frequency), exponential/nonlinear force loading is essential. In the high wind speed region, simpler linear loading methods can be adopted.

It was also found that the static displacement caused by medium-to-high wind speeds (6 m/s) is nearly identical to that caused by low wind speeds (2 m/s); however, such high-frequency vibrations significantly increase the fatigue risk of transmission lines. Therefore, in engineering design, safety assessments should not rely solely on displacement but must also consider the fatigue effects of high-frequency vibrations.

Through comparison, it was observed that the wind load on the robot-transmission

line coupling system is proportional to the square of the wind speed, regardless of whether the span is 300 m or 5 m. Regardless of the span size, the wind force per unit length of the transmission line remains constant, as does the wind load on the robot. This indicates that although the span lengths differ, the coupling effect between the unit transmission line and the robot remains fundamentally consistent. This validates that the experimental system, despite utilizing a 5-m span, can effectively verify coupling vibration characteristics under various wind disturbances.

Furthermore, regardless of whether the transmission line span is 300 m or 5 m, the vortex-induced frequency at the coupling point is 16.8 Hz at a wind speed of 2 m/s and 50.4 Hz at 6 m/s. Consequently, the vortex-induced frequency is proportional to the wind speed. At low wind speeds (2 m/s), the vortex-induced frequency approaches the structural high-frequency state, making it prone to harmonic resonance with the fundamental frequency of 1.57 Hz. Severe coupling vibrations can easily occur if external loads are applied directly under these conditions. To mitigate coupling vibrations in low wind speed states, a nonlinear contact force strategy is necessary. Conversely, at medium-to-high wind speeds (6 m/s), the vortex-induced frequency is significantly higher than the fundamental frequency of the structure. The wind load generates high-frequency forced vibration, which cannot effectively excite the low-frequency response of the structure; thus, coupling vibration is minimal, and a linear contact force strategy is more effective for suppression. Therefore, dynamically adjusting the loading mode based on the wind speed-frequency relationship is essential for the control strategy, rather than simply increasing the control force.

## 6. Conclusion

In this study, a coupling vibration model of the HVTIR-line system under wind disturbance was constructed. Based on this model, contact force control strategies for varying wind conditions were derived: an exponential nonlinear contact force model was employed at low wind speeds, while a linear contact force model was adopted for medium-to-high wind speeds. The theoretical support provided here supports the smooth landing of the HVTIR.

The experiments in this study utilized a small span and fans to simulate wind loads, which differ from actual field conditions. Future work will involve collecting data in real-world environments to refine the HVTIR-line coupling model during wind disturbances and enhance its accuracy. These models and control strategies are capable of guiding the HVTIR to land smoothly on transmission lines and can be used to inversely optimize the design of the HVTIR and transmission line system.

**Author contributions:** Conceptualization, XZ and HS; methodology, HS; software, HS and ABA; validation, HS, XZ and HX; formal analysis, HS and ABA; investigation, XZ, HS, ABA and HX; resources, HS and ABA; data curation, XZ and HS; writing—original draft preparation, XZ and HS; writing—review and editing, XZ and HS; visualization, XZ and HS; supervision, HX and HS; project administration, XZ and HX; funding acquisition, XZ and HX. All authors have read and agreed to the published version of the manuscript.

**Funding:** This research was funded by the Key Research and Development Plan of Shaanxi Province, China, grant number 2018ZDXM-GY-093.

**Institutional review board statement:** Not applicable.

**Informed consent statement:** Not applicable.

**Data availability statement:** Not applicable.

**Conflict of interest:** The authors declare no conflict of interest.

## References

1. Alhassan AB, Zhang X, Shen H, et al. Power transmission line inspection robots: A review, trends and challenges for future research. International Journal of Electrical Power & Energy Systems. 2020; 118: 105862. doi: 10.1016/j.ijepes.2020.105862
2. Wang Y, Qin X, Jia W, et al. Multiobjective Energy Consumption Optimization of a Flying–Walking Power Transmission Line Inspection Robot during Flight Missions Using Improved NSGA-II. Applied Sciences. 2024; 14(4): 1637. doi: 10.3390/app14041637
3. Chao C, Mei X, Wei Y, et al. A balanced walking-clamp mechanism for inspection robot of transmission line. Industrial Robot: The International Journal of Robotics Research and Application. 2023; 50(4): 673–685. doi: 10.1108/IR-09-2022-0226
4. Luo Y, Yu X, Yang D, et al. A survey of intelligent transmission line inspection based on unmanned aerial vehicle. Artificial Intelligence Review. 2023; 56(1): 173–201. doi: 10.1007/s10462-022-10189-2
5. Zhang X, Shen H, Alhassan AB, et al. Coupling vibration analysis for inspection robot landing on high voltage transmission line. Sound & Vibration. 2025; 59(5). doi: 10.59400/sv3788
6. Zhang X, Shen H, Alhassan AB, et al. Gripper vibration analysis of inspection robot during variable working flight of pre-landing on high-voltage transmission line. Journal of Mechanical Science and Technology. 2024; 38(3): 1411–1428. doi: 10.1007/s12206-024-0233-7
7. Chermprayong P, Zhang K, Xiao F, et al. An Integrated Delta Manipulator for Aerial Repair: A New Aerial Robotic System. IEEE Robotics & Automation Magazine. 2019; 26: 54–66.
8. Suarez A, Real F, Vega VM, et al. Compliant Bimanual Aerial Manipulation: Standard and Long Reach Configurations. IEEE Access. 2020; 8: 88844–88865. doi: 10.1109/ACCESS.2020.2993101
9. Paul H, Miyazaki R, Ladig R, et al. TAMS: development of a multipurpose three-arm aerial manipulator system. Advanced Robotics. 2021; 35(1): 31–47. doi: 10.1080/01691864.2020.1845237
10. Li L, Zhang T, Zhong H, et al. Autonomous Removing Foreign Objects for Power Transmission Line by Using a Vision-Guided Unmanned Aerial Manipulator. Journal of Intelligent & Robotic Systems. 2021; 103(2): 23. doi: 10.1007/s10846-021-01482-3
11. Zhang Z, Chen Y, Wu Y, et al. Gliding grasping analysis and hybrid force/position control for unmanned aerial manipulator system. ISA Transactions. 2022; 126: 377–387. doi: 10.1016/j.isatra.2021.07.038
12. Meng X, He Y, Han J. Hybrid Force/Motion Control and Implementation of an Aerial Manipulator towards Sustained Contact Operations. In: Proceedings of the 2019 IEEE/RSJ International Conference on Intelligent Robots and Systems (IROS); 3–8 November 2019; Macau, China. pp. 3678–3683. doi: 10.1109/IROS40897.2019.8967808
13. Wang T, Umemoto K, Endo T, et al. Modeling and Control of a Quadrotor UAV Equipped With a Flexible Arm in Vertical Plane. IEEE Access. 2021; 9: 98476–98489. doi: 10.1109/ACCESS.2021.3095536
14. Khanmirza E, Daneshjou K, Ravandi AK. Underactuated Flexible Aerial Manipulators: a New Framework for Optimal Trajectory Planning Under Constraints Induced by Complex Dynamics. Journal of Intelligent & Robotic Systems. 2018; 92(3–4): 599–613. doi: 10.1007/s10846-017-0711-6
15. Orozco Soto SM, Lippiello V. Increasing Horizontal Controlled Force Delivery Capabilities of Aerial Manipulators by Leveraging the Environment. Robotics. 2024; 13(10): 147. doi: 10.3390/robotics13100147
16. Acosta JÁ, De Cos CR, Ollero A. Accurate control of Aerial Manipulators outdoors. A reliable and self-coordinated nonlinear approach. Aerospace Science and Technology. 2020; 99: 105731. doi: 10.1016/j.ast.2020.105731
17. Ikeda T, Ohara K, Ichikawa A, et al. Aerial Manipulator Control Method Based on Generalized Jacobian. Journal of

Robotics and Mechatronics. 2021; 33(2): 231–241. doi: 10.20965/jrm.2021.p0231
18. Lee D, Seo H, Jang I, et al. Aerial Manipulator Pushing a Movable Structure Using a DOB-Based Robust Controller. IEEE Robotics and Automation Letters. 2021; 6(2): 723–730. doi: 10.1109/LRA.2020.3047779
19. Nava G, Sable Q, Tognon M, et al. Direct Force Feedback Control and Online Multi-Task Optimization for Aerial Manipulators. IEEE Robotics and Automation Letters. 2020; 5(2): 331–338. doi: 10.1109/LRA.2019.2958473
20. Fang Q, Mao P. Compliant Contact Force Control for Aerial Manipulator of Adaptive Neural Network-Based Robust Control. Sensors. 2024; 24(8): 2556. doi: 10.3390/s24082556
21. Zhang G, He Y, Dai B, et al. Aerial Grasping of an Object in the Strong Wind: Robust Control of an Aerial Manipulator. Applied Sciences. 2019; 9(11): 2230. doi: 10.3390/app9112230
22. Liu Y-C, Huang C-Y. DDPG-Based Adaptive Robust Tracking Control for Aerial Manipulators With Decoupling Approach. IEEE Transactions on Cybernetics. 2022; 52(8): 8258–8271. doi: 10.1109/TCYB.2021.3049555
23. Jiao R, Chou W, Rong Y, et al. Anti-Disturbance Control for Quadrotor UAV Manipulator Attitude System Based on Fuzzy Adaptive Saturation Super-Twisting Sliding Mode Observer. Applied Sciences. 2020; 10(11): 3719. doi: 10.3390/app10113719
24. Bodie K, Tognon M, Siegwart R. Dynamic End Effector Tracking With an Omnidirectional Parallel Aerial Manipulator. IEEE Robotics and Automation Letters. 2021; 6(4): 8165–8172. doi: 10.1109/LRA.2021.3101864
25. Malczyk G, Brunner M, Cuniato E, et al. Multi-directional Interaction Force Control with an Aerial Manipulator Under External Disturbances. Autonomous Robots. 2023; 47(8): 1325–1343. doi: 10.1007/s10514-023-10128-2
26. Tang Y, Duan Z, Xu F, et al. Probabilistic Model of Random Equivalent Static Wind Loads on Transmission Line Cables Under Strong Winds. Engineering Mechanics. 2024; 41(1): 124–137.
27. Desai YM, Yu P, Popplewell N, et al. Finite element modelling of transmission line galloping. Computers & Structures. 1995; 57(3): 407–420. doi: 10.1016/0045-7949(94)00630-L
28. Alhassan AB, Zhang X, Shen H, et al. Precise Motion Control of a Power Line Inspection Robot Using Hybrid Time Delay and State Feedback Control. Frontiers in Robotics and AI. 2022; 9: 746991. doi: 10.3389/frobt.2022.746991